Machulla and Heinz highlight promising applications of novel radioligands for PET brain imaging of the κ-opioid receptor system in neuropsychiatric disorders. . . . . ***Page 386***

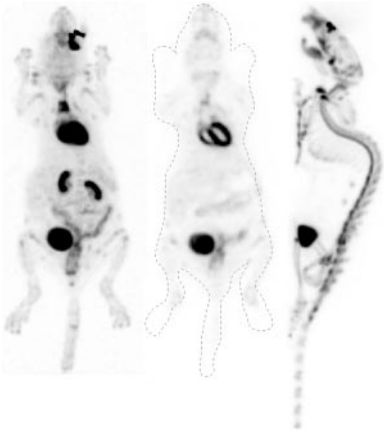

Mariani and colleagues review the current state of intraoperative γ-probes for radioguided surgery, including features that nuclear medicine physicians and surgeons should consider when choosing probes. . . . . ***Page 388***

Sharkey surveys the rapidly evolving technologies of pretargeting and questions that remain about the mechanism by which such procedures enhance and improve therapeutic outcomes. . . . . ***Page 391***

Classe and colleagues evaluate the performance of 3 commercially available γ-probes in axillary sentinel lymph node detection in a large group of patients with early breast cancer. . . . . ***Page 395***

van Westreenen and colleagues investigate the feasibility of ^{18}F-FLT as a PET tracer for the detection and staging of esophageal cancer and compare its performance with that of ^{18}F-FDG. . . . . ***Page 400***

Yen and colleagues report on the potential of ^{18}F-FDG PET to identify distant metastases when staging patients with nasopharyngeal carcinoma, an epithelial malignancy with high frequency in some areas of China. . . . . ***Page 405***

Pauleit and colleagues discuss the results of a prospective study comparing the potential efficacy of ^{18}F-FET and ^{18}F-FDG in PET imaging of patients with a variety of suspected malignant peripheral tumors. . . . . ***Page 411***

Acampa and colleagues compare the prognostic value of predischarge dobutamine stress echocardiography and dobutamine myocardial SPECT perfusion imaging in patients with prior myocardial infarction. . . . . ***Page 417***

Jaskowiak and colleagues evaluate the effects of changes in the number of iterations in the OSEM reconstruction process on average standardized uptake and maximum standardized uptake values in studies acquired with PET/CT. . . . . ***Page 424***

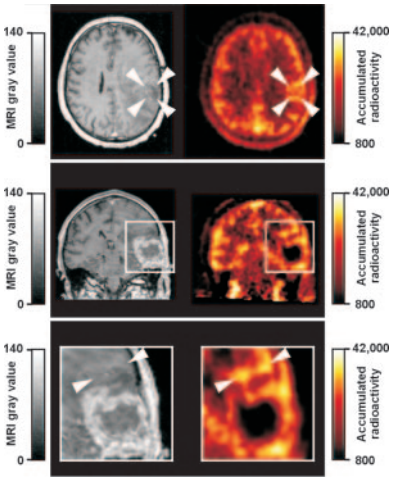

Beyer and colleagues compare several intravenous contrast injection protocols for routine whole-body PET/CT, with a goal of reducing the common occurrence of high-density imaging artifacts. . . . . ***Page 429***

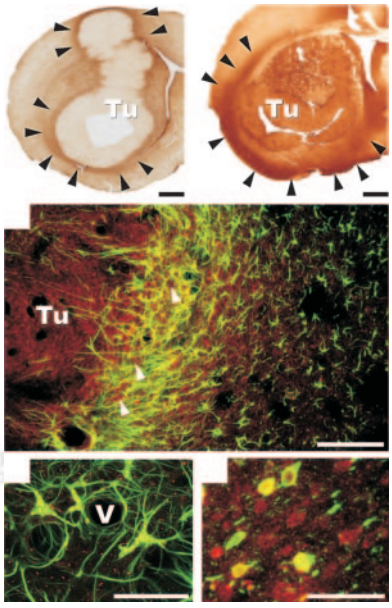

DiFilippo and Brunken assess the effect of pacemaker leads and implantable cardioverter defibrillator leads on the accuracy of cardiac PET/CT and discuss potential software-based correction algorithms. . . . . ***Page 436***

Keidar and colleagues investigate the ability of PET/CT to accurately differentiate between osteomyelitis and soft-tissue infection in the diabetic foot. . . . . ***Page 444***

Bauer and colleagues report on the molecular imaging utility of ^{18}F-CPFPX, a novel PET tracer, as a potential indicator of local cerebral response to tumor invasion in a glioma-bearing rat model. . . . . ***Page 450***

Tai and colleagues evaluate the basic performance of a new-generation, scintillator-based small-animal PET scanner and compare it with previous models. . . ***Page 455***

Elgqvist and colleagues describe the myelotoxicity and relative biologic effective-

ness of the α-emitter ^{211}At conjugated to monoclonal antibodies in a mouse model and compare the results with those from ^{99m}Tc-monoclonal antibodies and external radiation from a ^{60}Co source. . . ***Page 464***

Lee and colleagues examine the biodistribution of radiolabeled RGD peptides and expression of α_v integrin in a mouse model of hindlimb ischemia, with a goal of assessing the method's potential for noninvasive monitoring of peripheral ischemic lesions. . . . . ***Page 472***

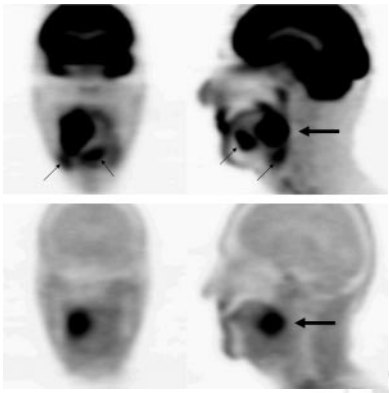

Kang and colleagues report on the development of a transgenic mouse model in which the sodium/iodide symporter is expressed as an imaging reporter gene only in cardiomyocytes, as a step toward γ-camera and microPET imaging of cellular differentiation in vivo. . . . . ***Page 479***

Talbot and colleagues describe the results of experiments in baboons to assess the potential of the radioligand ^{11}C-GR103545 for PET imaging of brain κ-opioid receptors. . . . . ***Page 484***

van Schaijk and colleagues outline an efficient, 2-step pretargeting strategy for treatment of renal cell carcinoma based on a biologically produced bispecific monoclonal antibody in mouse models and discuss the effects of physiologic characteristics of tumors in pretargeting strategies. . . . . ***Page 495***

Thomas and colleagues use new data specifically acquired to address the issue of testicular uptake, as well as reevaluations of extant data for biodistribution in other organs, to derive revised radiation dosimetry estimates for ^{201}Tl-thallous chloride. . . . . ***Page 502***

Nakamura and colleagues investigate the antisense targeting of P-glycoprotein expression in vitro and suggest a potential application for antisense imaging of multidrug resistance in cancer. . . . ***Page 509***

Jimenez and colleagues assess coronary vascular smooth muscle cell proliferation in a swine transplant model by imaging regions of uptake of an ^{111}In-labeled monoclonal antibody, a method with promise for early noninvasive detection of transplant vasculopathy. . . . . ***Page 514***

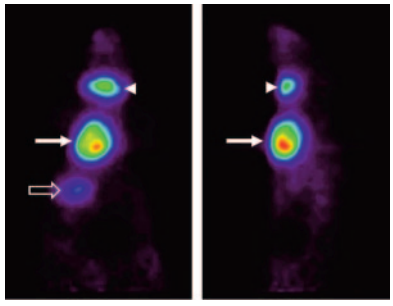

Antoch and colleagues compare the utility of imaging normal liver tissue with contrast-enhanced ultrasound, CT, MRI, ^{18}F-FDG PET, and PET/CT in patients immediately after radiofrequency ablation. . . . . ***Page 520***

Bennink and colleagues evaluate dedicated animal pinhole SPECT for the in vivo study of inflammatory activity and neutrophil recruitment in experimental colitis. . . . . ***Page 526***

Kersemans and colleagues investigate the distribution and accumulation characteristics of the tracer ^{123}I-2-iodo-L-phenylalanine as a specific tumor tracer for SPECT in 2 mouse models. . . . . ***Page 532***

Bouilleret and colleagues report on studies with PET to elucidate the involvement of dopamine neurotransmission in different epileptic syndromes and provide direct evidence of basal ganglia involvement in human epilepsy. . . . . ***Page 540***

ON THE COVER

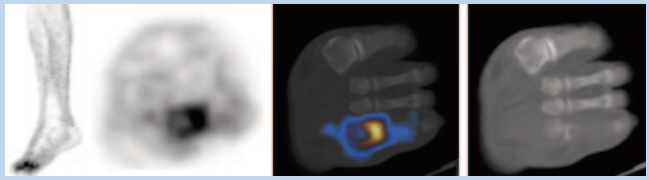

In this 50-y-old man with a nonhealing wound in the right forefoot, osteomyelitis complicating diabetic foot was diagnosed on the basis of PET/CT findings. From left to right, ^{18}F-FDG PET coronal and transaxial images show an area of increased ^{18}F-FDG uptake in the lateral aspect of the forefoot, PET/CT image localizes abnormal ^{18}F-FDG uptake to the head of the fourth metatarsus, and CT image shows normal bone structure in corresponding area. Osteomyelitis was further confirmed by histopathologic examination of tissue samples obtained at surgery.